

Article

Monitoring Surface Soil Moisture Content over the Vegetated Area by Integrating Optical and SAR Satellite Observations in the Permafrost Region of Tibetan Plateau

Chenyang Xu ^{1,*} , John J. Qu ¹ , Xianjun Hao ¹  and Di Wu ²

¹ Global Environment and Natural Resources Institute (GENRI) and Department of Geography and GeoInformation Science (GGS), College of Science, George Mason University, Fairfax, VA 22030, USA; jqu@gmu.edu (J.J.Q.); xhao1@gmu.edu (X.H.)

² China Three Gorges International Corporation, Xicheng District, Beijing 100022, China; wu_di@ctg.com.cn

* Correspondence: cxu8@masonlive.gmu.edu; Tel.: +1-703-678-5092

Received: 7 December 2019; Accepted: 30 December 2019; Published: 3 January 2020



Abstract: Surface soil moisture (SSM), the average water content of surface soil (up to 5 cm depth), plays a key role in the energy exchange within the ecosystem. We estimated SSM in areas with vegetation cover (grassland) by combining microwave and optical satellite measurements in the central Tibetan Plateau (TP) in 2015. We exploited TERRA moderate resolution imaging spectroradiometer (MODIS) and Sentinel-1A synthetic aperture radar (SAR) observations to estimate SSM through a simplified water-cloud model (sWCM). This model considers the impact of vegetation water content (VWC) to SSM retrieval by integrating the vegetation index (VI), the normalized difference water index (NDWI), or the normalized difference infrared index (NDII). Sentinel-1 SAR C-band backscattering coefficients, incidence angle, and NDWI/NDII were assimilated in the sWCM to monitor SSM. The soil moisture and temperature monitoring network on the central TP (CTP-SMTMN) measures SSM within the study area, and ground measurements were applied to train and validate the model. Via the proposed methods, we estimated the SSM in vegetated area with an R^2 of 0.43 and a ubRMSE of $0.06 \text{ m}^3/\text{m}^3$ when integrating the NDWI and with an R^2 of 0.45 and a ubRMSE of $0.06 \text{ m}^3/\text{m}^3$ when integrating the NDII.

Keywords: surface soil moisture; optical; microwave; vegetation cover; NDWI; NDII; Tibetan Plateau

1. Introduction

Soil moisture (SM) plays a key role in evapotranspiration as well as the water dynamics and energy transfer between land and the atmosphere [1–7]. SM has been assimilated in various land surface models (LSM) and atmospheric models to predict weather, drought, flood, and climate trends [6,8,9]. Understanding the spatial and temporal distribution of SM can therefore help us better analyze the regional and global water dynamics and improve the hydrology related models. Root zone SM (RZSM), defined as the SM at a depth from 0.5 to 1 m, is crucial for crop production and serves as an indicator for crop yield estimation [10,11]. However, RZSM cannot be monitored through satellite techniques currently. In contrast, surface soil moisture (SSM) is defined as the SM up to a depth of 5 cm and represents the interface between land and the atmosphere [5–8], various methods have been proposed to estimate SSM using satellite observations. We applied satellite measurements in this study to monitor SSM over the central of Tibetan Plateau (TP), since SSM plays a key role in regulating the energy and water transfer between land and atmosphere and has a significant impact on the regional climate of TP.

The cosmic-ray soil moisture observing system (COSMOS) allows to directly measure SM at various depths [12]. However, such point-based measurements do not fully reflect the overall situation, since SM shows a high spatial and temporal heterogeneity [6,9,12]. To overcome this limitation, remote sensing techniques have been used to provide spatial and temporal continuous land surface observation and are widely applied in SSM monitoring [6,9]. Currently, optical, thermal, and microwave methods are available [6,9].

When SM increases, the reflectance decreases inversely for solar band with wavelength from 0.4 to 2.5 μm . That is to say, surface soil with high water content is darker. This is the physical principle for estimating SSM with optical methods [6,9]. Various experiments and approaches have been conducted to describe the relationship between surface soil reflectance and its water content [13–15]. The thermal methods depend on the change of soil surface temperature with different SSM. Thermal inertia method only considers thermal bands, temperature/vegetation index method analyzes solar reflective bands and thermal emissive bands together [9,16,17]. However, both optical and thermal bands are affected by weather conditions, cannot be used when there is a cloud cover. For instance, the 16-day revisit cycle of Landsat 8 makes it difficult to collect enough valuable observations within a specific study period. And, the optical/thermal bands have limited penetration, they are therefore only feasible within bare soil under clear sky. However, monitoring SSM in a vegetated area is of great importance, since SSM is an important parameter for agricultural drought monitoring and has been widely applied in many LSM over vegetated areas.

In contrast, microwave techniques can be used under any weather condition using the electromagnetic radiation in the microwave region (0.5–100 cm) [6,9,18]. Both passive and active microwave sensors have been widely applied to monitor SSM [6,9,18]. Passive microwave sensors collect signals emitted by soil, while active microwave sensors send a pulse and analyze the soil reflected signal. Previous research works have shown that passive microwave sensors can be used to monitor global SSM through measuring the intensity of microwave emissivity from the soil [19–22]. Currently used passive microwave sensors for SSM measurements include the scanning multi-channel microwave radiometer (SMMR), the special sensor microwave imager (SSM/I), the advanced microwave scanning radiometer for EOS (AMSR-E), soil moisture and ocean salinity (SMOS), and soil moisture active passive (SMAP) [9,19–22]. Although showing a good temporal resolution (1–2 day), the main limitation of passive microwave methods is the coarse spatial resolution (10–35 km), making them unsuitable for applications at the fine scale.

Great progress has been made in mapping regional soil moisture with active microwave sensors, a microwave pulse that is sensitive to SM is sent and received [6,11]. SSM is estimated based on the difference between sent and received signals [23]. The active microwave remote sensing approaches such as synthetic aperture radar (SAR) with fine spatial resolutions (5–30 m), enable SSM monitoring at finer spatial scales. The SAR monitors SSM with three microwave bands: X-band (~3 cm), C-band (~6 cm), and L-band (~24 cm). Of these, the L-band has the strongest penetration, while X-band has the weakest penetration [4,24,25]. Microwave signals with longer wavelengths as L-band can penetrate the canopy and are reflected by the soil surface [4]. Currently, there are some SAR systems which are suitable for SM retrieval: the European remote-sensing satellite (ERS)-1/2/3 C-band, RADARSAR-1/2 C-band, advanced land observation satellite (ALOS), the phased array type L-band synthetic aperture radar (PALSAR), TerraSAT X-band (TSX), Sentinel-1/2/3 C-band (5.404 GHz) [26–30]. In this study, we used the Sentinel-1A SAR with moderate penetration of the C-band signal for the grassland area.

In the past few decades, SAR has been widely used to monitor SSM [28,31–49]. There is a strong relationship between the C-band backscattering coefficient and SSM, making the C-band backscattering coefficient an effective tool to estimate SSM. However, the relationship between backscattering coefficients and SSM varies significantly under different surface types and vegetation features [31–36,38,39,43–49]. Artificial neural network (ANN) and support vector machine (SVM) have been combined with regression algorithms to retrieve vegetated SSM [31–35]. Because of the concerns about vegetation characteristics, some vegetation backscattering models have been established to

describe the contribution of vegetation, with the most widely used on being the water-cloud model (WCM). Based on the radiative transfer theory, the contribution of vegetation was modeled by considering both the volume scattering produced by vegetation and the attenuation effect of soil under vegetation on the backscattering. The total backscattering of the of the vegetated surface was derived from the backscattering of bare surface using the WCM [31–36,38,39,43–49]. The model simulated the backscattering of vegetated surfaces as a function of soil backscattering and the vegetation water content (VWC) [31–49].

Wang et al. integrated the advanced integral equation model (AIEM) with WCM to estimate SSM over vegetated area. However, it is still under debate which vegetation parameter is the most suitable one to estimate vegetation canopy backscattering in the WCM model. One of the major factors that affect the canopy backscattering is the VWC [40–42,44,45,48]. Several vegetation indices (VI) have been successfully applied to retrieve canopy VWC for grassland and agricultural areas [49–54]. The normalized difference vegetation index (NDVI) has been widely applied to monitor vegetation conditions and has been assimilated into the WCM to take the effects of the canopy on soil surface backscattering into consideration [48,49]. However, the NDVI is not the most suitable VI to be assimilated in the WCM, mainly because it is calculated based on the reflectance of the red band and the near-infrared band. The variation of the canopy's influence on surface backscattering is mainly based on the VWC, while the red band is not that sensitive to VWC compared with shortwave infrared bands, as shown in Figure 1 [55]. Previous studies pointed out that two VIs, the normalized difference water index (NDWI), and the normalized difference infrared index (NDII) can be applied to monitor canopy VWC for various vegetation types with good results through linear or nonlinear models since they target the strong water absorption features of shortwave-infrared bands [53–58]. In this study, we applied both NDWI and NDII in the WCM to estimate SSM by considering the influence of vegetation canopy backscattering. Bao et al. tried to use Landsat retrieved VI to estimate VWC [49]. However, with Landsat 8 has the 16-day revisit cycle, and Sentinel-1A with the 12-day revisit cycle, there is always a 2–6 day time interval between Landsat 8 and Sentinel overpassing day, which makes it a big issue to fill the time gap. Landsat 8 is very sensitive to cloud cover, only limited valid satellite observations can be collected. In this study, we applied the daily MODIS reflectance products instead of combining the Sentinel-1 products on the same observing.

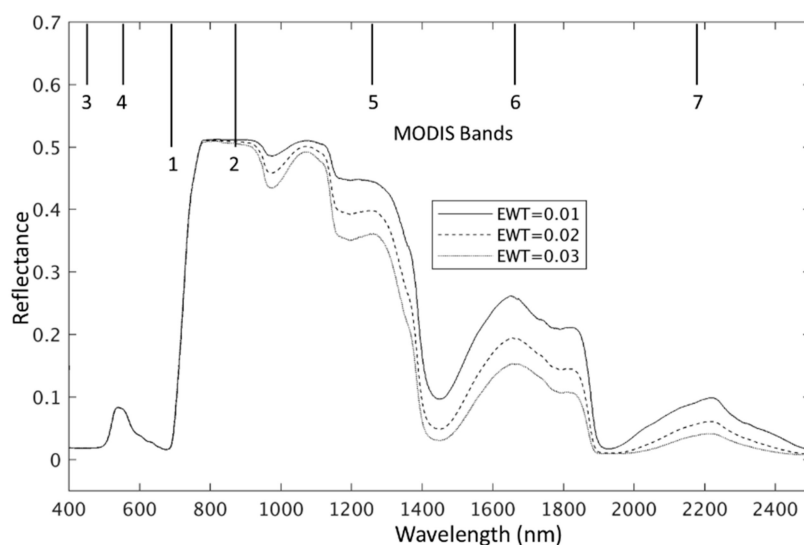


Figure 1. Spectral reflectance simulated for MODIS bands, where EWT represents equivalent water thickness (EWT, cm).

The Tibetan Plateau, the highest plateau on earth, contains a large amount of permafrost soil, widely distributed. The energy and water dynamics on this plateau is very sensitive to the climate

change on the Asian continent and, subsequently, on a global scale. TP makes the monsoon on its southwestern side weaken in the summer, while the drought in central Asia consequently intensifies. The heat rising by TP in summer strengthens atmospheric circulation, and the SM condition in TP acts as an amplifier for the drought in central Asia and the monsoon in East Asia. Against the background of a changing climate, the thawing of the permafrost layer with grassland as the main vegetation type will considerably impact the water dynamics on the TP. Based on previous studies, the soil energy–water distribution and freezing–thawing processes vary spatially, and estimating SM at high spatial and temporal resolution is of great importance to develop protection measures for the plateau [59,60]. In this context, we estimated volumetric SSM (m^3/m^3) with vegetation cover (grassland) in the central of the TP, based on a simplified WCM (sWCM) through the soil backscattering coefficient and signal incident angle, which can be extracted from Sentinel-1 products. Since in the winter (from December to February) the soil was completely frozen, the study was conducted in spring, summer, and winter (from March to November). To eliminate the impact of backscattering coefficients from vegetation canopy, we integrate VI (NDII and NDWI) in the WCM. Both NDII and NDWI can be derived through MODIS shortwave infrared and near infrared bands. To better understand soil properties on the TP, including ST and SM at various depths, an in situ measurement network has been built in Naqu, the center of the TP, providing temporal continuous ST and SM data at four depths. We validated the retrieval method with ground measurements to demonstrate the feasibility and performance.

2. Study Area

TP is the highest plateau in the world with an average elevation of over 4000 m above sea level. Our study area is located within the center of the TP ($31\text{--}32^\circ\text{N}$, $91.5\text{--}92.5^\circ\text{E}$), covering about 10,000 km^2 . As shown in Figure 2a,b, the study area is relatively flat, with several hills distributed. As shown in Figure 2c, over 95% of the study area is grassland, mainly alpine grasslands, but also prairie and meadows [60,61]. The growing season is short, allowing a grass height of only several centimeters [7,60], facilitating the application of remote sensing techniques in this area. The soil types are mainly silt and sand, with a clay content of less than 10%, resulting in a high drainage effect. The climate is semiarid, with an annual precipitation of about 500 mm, mostly concentrated in summer. According to long-term records, around 75% of the precipitation occurs from June to August [7,60,61]. SM shows a strong seasonal behavior, especially in terms of SSM. The annual freeze/thaw cycle considerably influences the soil water dynamics in the area, impacting SSM measurements. The annual freeze and thaw cycle of the study area starts to freeze in October, and it starts to thaw in January. From December to February, the soil surface is fully frozen. Therefore, the ground measurements were conducted from March and November.

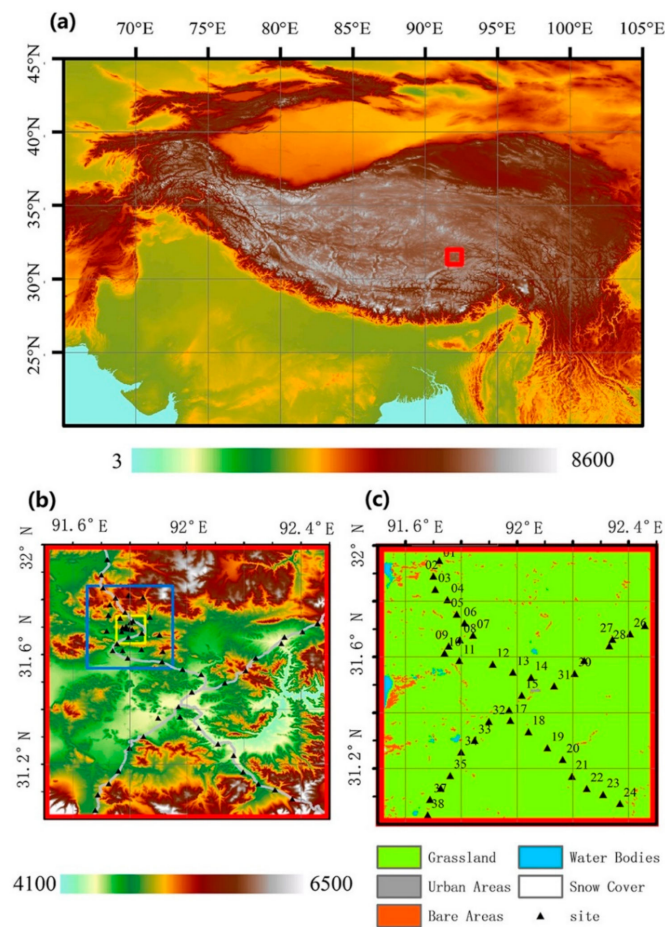


Figure 2. (a) Relative location of the study area on the Tibetan Plateau (TP) (indicated by the red square). (b) Locations of all sampling stations within a $1^\circ \times 1^\circ$ area on the central TP, with blue and yellow squares representing the $0.3^\circ \times 0.3^\circ$ and $0.1^\circ \times 0.1^\circ$ networks, respectively. (c) Distribution of the sampling stations with the land cover type [61].

3. Data and Methodology

3.1. Data

We applied TERRA MODIS reflectance to generate two vegetation indices (VI) since one of the shortwave infrared bands of MODIS, band 6, has broken down and cannot be applied to calculate NDII. The Sentinel-1A SAR incident angle and backscattering coefficients of the land surface were combined with each VI separately to build the sWCM. Two thirds of the in situ SSM measurements collected from the CTP-SMTMN were used to train the sWCM proposed in this study, while one third of the measurements was applied for model validation.

3.1.1. In Situ Measurements

Based on the significance of the TP for the global climate, several in situ measurement networks have been established there in the last few decades to investigate the soil–vegetation–atmosphere cycle and its relationship with the local climate [61]. In this study, we used in situ data collected from a multiscale soil moisture and temperature monitoring network in the central Tibetan Plateau (CTP-SMTMN) established by the Data Assimilation and Modeling Center for Tibetan Multi-Spheres (DAM) to evaluate SSM. There are 56 sampling sites in total at three spatial scales, measuring SM and ST at three spatial scales (1° , 0.3° , 0.1°) and four depths (0–5, 10, 20, 40 cm) from 1 August 2010 to 30 June 2016. The sensors automatically measured SM and ST every 30 minutes, calculating the average

values for the past 30 minutes. The in situ measurements were validated by taking 10 undisturbed soil samples from different stations [60]. We used a large-scale network in this study, and randomly selected observations of 18 sampling sites to train the model proposed in this study; we also used observations of another eight sampling sites to validate the results retrieved by the sWCM. The geolocation of the sampling sites used for training and validation are listed in Tables 1 and 2, respectively.

Table 1. Geolocations of 18 sampling sites used for model training.

Site #	Longitude (°E)	Latitude (°N)	Altitude (m)	Major Soil Type
BC05	92.20	31.17	4548	Sand (49.46%)
CD02	92.41	31.68	4612	Silt (57.98%)
CD03	92.34	31.66	4518	Silt (51.59%)
CD06	92.21	31.54	4769	Silt (50.85%)
MS3475	91.72	31.95	4637	Sand (62.02%)
MS3482	91.70	31.89	4713	Silt (64.89%)
MS3488	91.71	31.84	4799	Sand (56.52%)
MS3494	91.75	31.81	4818	Silt (56.20%)
MS3501	91.78	31.75	4723	Silt (54.95%)
MS3518	91.79	31.66	4574	Sand (55.13%)
MS3527	91.74	31.61	4552	Sand (66.44%)
MS3533	91.79	31.59	4539	Silt (60.85%)
MS3545	91.91	31.57	4671	Sand (54.55%)
MS3614	91.76	31.17	4633	Sand (48.84%)
MS3620	91.73	31.13	4765	Sand (48.68%)
MS3627	91.69	31.09	4736	Sand (71.69%)
MS3633	91.68	31.03	4675	Sand (51.81%)
MSBJ	91.90	31.37	4505	Sand (58.77%)

Table 2. Geolocations of eight sampling sites used for model validation.

Site #	Longitude (°E)	Latitude (°N)	Altitude (m)	Major Soil Type
BC03	92.31	31.11	4690	Silt (61.05%)
BC04	92.25	31.13	4609	Sand (56.13%)
BC08	92.04	31.33	4470	Sand (63.52%)
MS3523	91.75	31.64	4570	Sand (47.43%)
MS3501	91.78	31.75	4723	Silt (54.95%)
MS3552	91.98	31.55	4574	Silt (57.71%)
MS3559	92.05	31.53	4516	Sand (55.22%)
MS3603	91.80	31.26	4630	Silt (48.54%)

3.1.2. MODIS

We applied TERRA MODIS in this study. The MODIS is a land surface monitoring sensor launched by the National Aeronautics and Space Administration (NASA) on board the AQUA and TERRA satellites of the Earth Observing System (EOS) mission. MODIS has 36 spectral bands in total, monitoring land surface properties, ocean properties, atmosphere properties, among others. In this study, one near-infrared band (band 2) and two shortwave-infrared bands (band 5 and band 6) were chosen. We selected the MODIS daily 500-m surface reflectance products (MOD09GA) band 2 (841–876 μm) and band 6 (1628–1652 μm) to calculate NDII, band 2, and band 5 (1230–1250 μm) to calculate NDWI. The VIs were combined with Sentinel measurements in the sWCM to estimate vegetated SSM.

3.1.3. Sentinel-1 SAR

Since only the Sentinel-1A product covered our area in 2015, it was selected for our study. Compared with the MODIS product, the main advantage of Sentinel-1 is they can be acquired under all weather conditions, and Sentinel-1 radar sensors are not affected by cloud cover. Sentinel-1 carries a C-band (5.4 GHz) SAR sensor with multi-polarization imaging capability, which supports

both single polarization (HH, VV) and dual polarization (HH + HV, VV + VH). There are four imaging modes (stripmap model (SM), interferometric wide swath (IW), extra-wide swath (EW), and wave mode (WM)) for the Sentinel product, which mainly differentiate in the stripe width. The SM, IW, and EW are available in both single and dual polarization, while WV is only available in single polarization. The IW swath mode is the main acquisition mode over land and satisfied the majority of service requirements; for this reason, it was selected in our study. We applied the VV IW backscattering coefficients and incident angle measurement in the model proposed above to estimate SSM (<https://www.asf.alaska.edu/sar-data-sets/sentinel-1/>).

3.2. Methodology

We used one MODIS near-infrared band and two shortwave-infrared bands to calculate NDWI and NDII to represent VWC; the backscattering coefficients and incident angle were extracted from sentinel-1A SAR products. These parameters were assimilated into the simplified WCM (sWCM) to monitor SSM combining in situ measurements, as illustrated in Figure 3. Two-thirds of the ground measurements were used to train the model, while one-third were applied for model validation. For this, we randomly selected 18 sampling sites from CTP-SMTMN to train the semi-empirical sWCM and eight sampling sites for model validation.

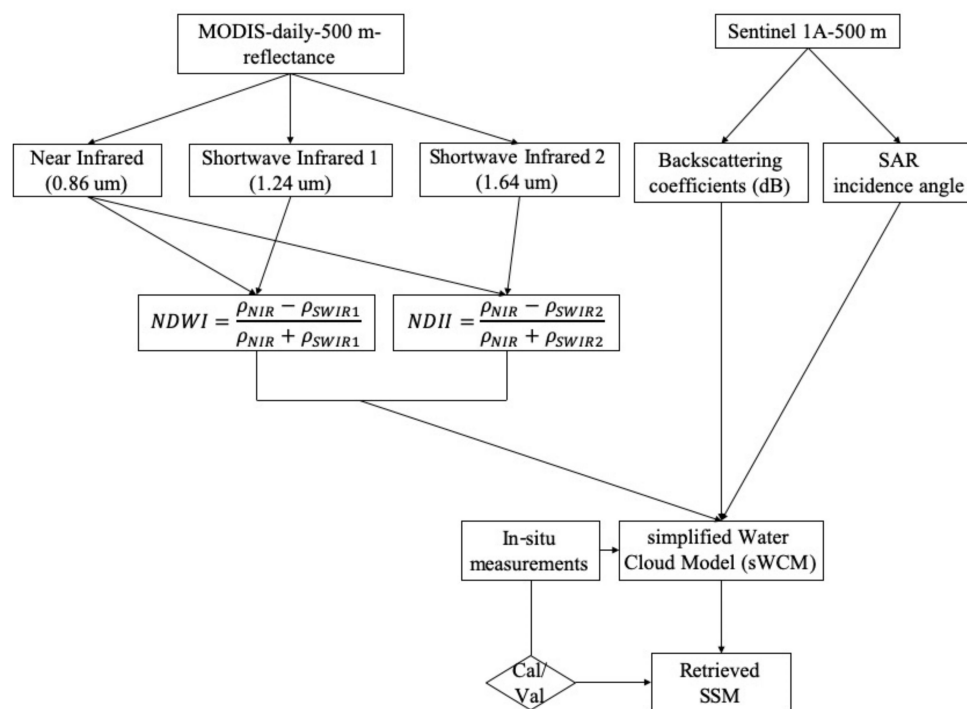


Figure 3. Flow chart of the main procedures.

The MODIS level-3 reflectance products were processed with the MODIS reprojection tool (MRT) conducted by NASA to subset the study area and projected to the UTM WGS84 46 zone with a 500-m spatial resolution. In addition, the Sentinel application platform (SNAP) was used to conduct the radiometric calibration/terrain calibration and to obtain the incident angle and backscattering coefficients that are required in the sWCM. The backscattering coefficients were generated through a linear conversion of the intensity of the microwave signal. Similar as in MODIS processing, SAR images were subset first to select the study area and were projected to UTM projection with a 500-m spatial resolution.

The main difference between NDII and NDWI is the wavelength of the selected shortwave-infrared band. The NDII applied near-infrared band with a wavelength of 860 μm and the shortwave-infrared

band with a wavelength of 1640 μm as illustrated in Equation (1), while NDWI applied the same near-infrared band and shortwave infrared band with a wavelength of 1240 μm as illustrated in Equation (2). We calculated both NDII and NDWI through the MODIS reflectance product and applied them in the WCM separately to the estimated SSM:

$$NDII = \frac{\rho_{nir}(860 \mu\text{m}) - \rho_{swir1}(1640 \mu\text{m})}{\rho_{nir}(860 \mu\text{m}) + \rho_{swir1}(1640 \mu\text{m})} \quad (1)$$

$$NDWI = \frac{\rho_{nir}(860 \mu\text{m}) - \rho_{swir2}(1240 \mu\text{m})}{\rho_{nir}(860 \mu\text{m}) + \rho_{swir2}(1240 \mu\text{m})} \quad (2)$$

where ρ_{nir} represents the reflectance of the near-infrared bands, ρ_{swir} , ρ_{swir2} represents the reflectance of two shortwave-infrared bands separately.

There is a linear relationship between these two vegetation indices and the VWC, which has been verified by several studies conducted in agricultural and grassland areas [54,57,58]:

$$VWC = a * VI + b \quad (3)$$

where a and b are empirical parameters in the linear model.

To better describe the backscattering of the soil and vegetation in vegetated areas, the original WCM adapted in this study, proposed by Attema and Ulaby, is based on the radiation transport model, considering the vegetation canopy to be uniform, with horizontal clouds, and ignoring multiple scattering. The backscattering coefficient monitored by SAR C-band signals composes surface soil scattering and scattering reflected from the vegetation; the WCM is illustrated using Equations (4)–(6):

$$\sigma^0 = \sigma_{veg}^0 + c * \sigma_{soil}^0 \quad (4)$$

$$\sigma_{veg}^0 = A * VWC * \cos(\theta) * (1 - C) \quad (5)$$

$$C = \exp(-2 * B * VWC * \sec(\theta)) \quad (6)$$

where σ^0 is the surface backscattering, σ_{veg}^0 represents the vegetation canopy backscattering, σ_{soil}^0 represents surface soil backscattering, θ represents the SAR incident angle, and VWC can be estimated from Equation (1) to Equation (3). In this model, A and B are two empirical parameters that are applied to simulate the backscattering of vegetated surfaces as a function of the soil backscattering and the VWC. Previous studies have pointed out that the empirical parameters can be set as A equals to 0.0855 and B equals to 0.0126 at VV polarization through model assimilation [35].

Previous studies have shown that there is a good linear correlation between the soil backscattering coefficient and SSM. Therefore, the soil backscattering coefficient can be described by soil volumetric moisture SSM (Equation (7)) [48,49]:

$$SSM = c * \sigma_{soil}^0 + d \quad (7)$$

where c and d are empirical parameters in the linear model.

The coefficient of determination (R^2), bias, the root-mean-square error (RMSE), and unbiased RMSE were applied to evaluate the retrieved SSM results based on in situ measurements. These evaluators mentioned above were calculated via Equations (8)–(11):

$$R^2 = \frac{\sum_{i=1}^n (P_i - \bar{O})^2}{\sum_{i=1}^n (O_i - \bar{O})^2} \quad (8)$$

$$bias = \frac{\sum_{i=1}^n (O_i - P_i)}{n} \quad (9)$$

$$RMSE = \sqrt{\frac{1}{n} \sum_{i=1}^n (O_i - P_i)^2} \quad (10)$$

$$ubRMSE = \sqrt{(RMSE)^2 - (bias)^2} \quad (11)$$

where n is the number of observations for validation, P is the predicted results, O is the in situ observation, and \bar{O} average of all observed value.

4. Results and Discussion

We estimated vegetated SSM within the central TP through sWCM combining multi-source satellite observations (MOD09 and Sentinel-1A SAR) and in situ measurements from CTP-SMTMN. In situ measurements were also applied to validate the monitoring results. Based on the statistical results obtained for 2015 (Table 3), the sWCM integrating MODIS and SAR observations can be applied to effectively retrieve SSM in the study area. Both NDII and NDWI were suitable ($R > 0.6$) and can be integrated into the sWCM for SSM monitoring. The NDII worked relatively better, with a higher R^2 , a lower RMSE, and a lower ubRMSE. Both NDII-sWCM and NDWI-sWCM slightly overestimated SSM with positive bias values over the study. Tables 4 and 5 are the statistical results of NDII-sWCM and NDWI-sWCM, respectively.

Table 3. Statistical results of the methods proposed in this study (all sites), with R^2 (coefficient determination), RMSE (root-mean-square error) (m^3/m^3), ubRMSE (unbiased root-mean-square error) (m^3/m^3), and bias (m^3/m^3).

Vegetation Index Applied	R^2	RMSE (m^3/m^3)	ubRMSE (m^3/m^3)	bias (m^3/m^3)
NDII	0.4513	0.0609	0.0603	0.0085
NDWI	0.4264	0.0613	0.0607	0.0083

Table 4. Statistical results of NDII-sWCM (normalized difference infrared index- simplified water-cloud model) for each validation sites, with R^2 (coefficient determination), RMSE (root-mean-square error) (m^3/m^3), ubRMSE (unbiased root-mean-square error) (m^3/m^3), and bias (m^3/m^3).

Site #	RMSE (m^3/m^3)	ubRMSE (m^3/m^3)	bias (m^3/m^3)
BC03	0.0591	0.0589	-0.0051
BC04	0.087	0.0610	0.0620
BC08	0.0656	0.0654	0.0043
MS3501	0.0926	0.0470	0.0798
MS3523	0.0368	0.0368	-0.0005
MS3552	0.0347	0.0346	-0.0020
MS3559	0.0407	0.0392	-0.0112
MS3603	0.0389	0.0363	-0.0141

Table 5. Statistical results of NDWI-sWCM (normalized difference water index- simplified water-cloud model) for each validation sites, with R^2 (coefficient determination), RMSE (root-mean-square error) (m^3/m^3), ubRMSE (unbiased root-mean-square-error) (m^3/m^3), and bias (m^3/m^3).

Site #	RMSE (m^3/m^3)	ubRMSE (m^3/m^3)	bias (m^3/m^3)
BC03	0.0564	0.0553	0.0112
BC04	0.0941	0.0681	0.0650
BC08	0.0724	0.0507	-0.0521
MS3501	0.0839	0.0441	0.0714
MS3523	0.0308	0.0296	-0.0087
MS3552	0.0389	0.0389	0.0009
MS3559	0.0415	0.0407	-0.008
MS3603	0.0395	0.0371	0.0143

Figure 4a illustrates the scatterplots between observed and predicted SSM values, considering VI as NDII or NDWI separately (with 1:1 red line shown). Both NDII and NDWI overestimated SSM under low SSM conditions (in situ SSM < 0.15 m³/m³), and both VIs underestimated SSM under high SSM conditions (in situ SSM > 0.2 m³/m³). Figure 4b represents the histogram of the differences between observed and predicted SSM values, the value accumulated (over 70%) between −0.05 to 0.05 m³/m³ for NDII, between −0.06 to 0.07 m³/m³ for NDWI.

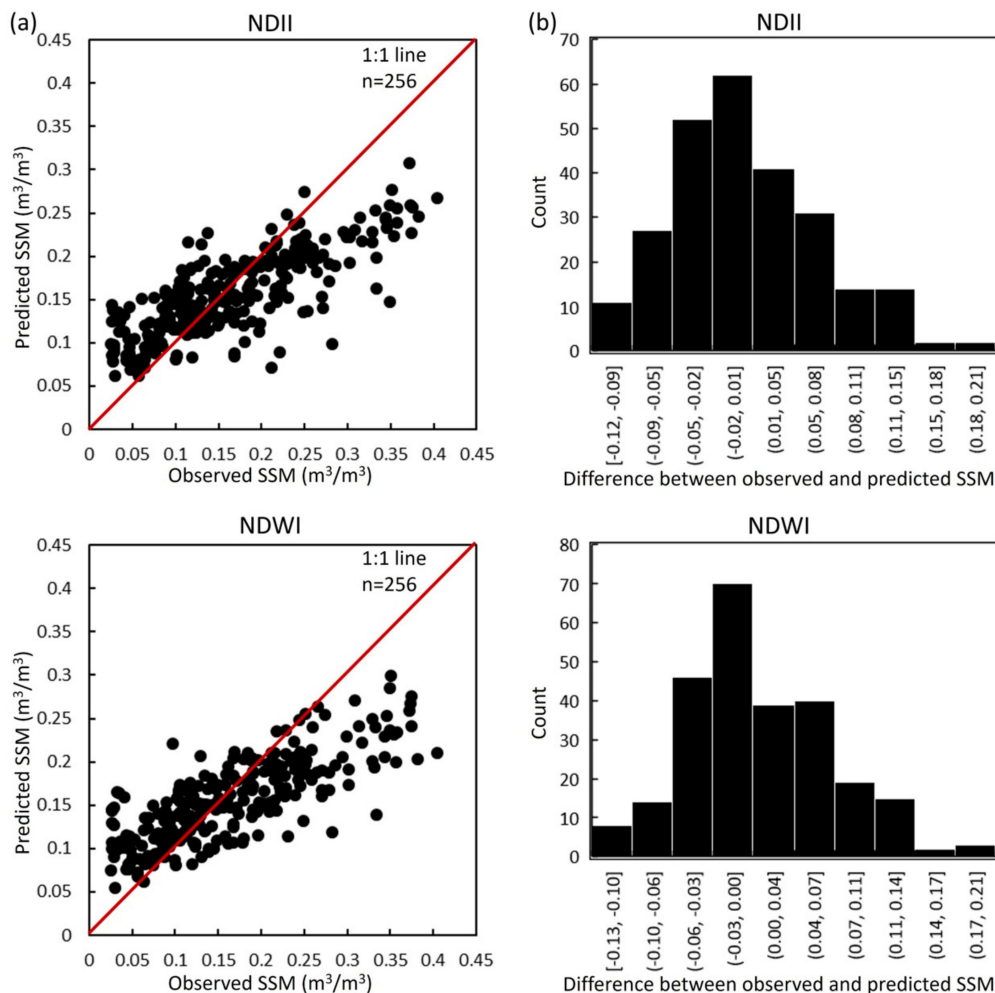


Figure 4. (a) Scatter plots for observed and predicted surface soil moisture (SSM) values using normalized difference infrared index (NDII) and normalized difference water index (NDWI), respectively. (b) Histogram showing the differences between observed and predicted SSM values using NDII and NDWI, respectively.

Figure 5a shows the time series of observed and predicted SSM values for eight validation sites separately. The red line represents the observed SSM values, green line represents the predicted SSM values with NDII integrated in sWCM, blue line represents the predicted SSM values with NDWI integrated in sWCM. For sites MS3552 and MS3603, the trend of predicted SSM (NDII-sWCM and NDWI-sWCM) matched the observed SSM quite well. For all sites, summer (May to August) has the highest SSM values which is consistent with the information provided above, that summer has the most precipitation within the year. Observed SSM values drop rapidly at the beginning of August for all sites, predicted SSM values of some sites drop rapidly at the same time. Such situation is not understood yet. Figure 5b,c illustrates the scatter plot between observed and predicted SSM values when NDII or NDWI were applied in the sWCM separately. In one site (BC08), sWCM overestimated SSM for the whole study period; while in two sites (BC04 and MS3501), sWCM underestimated SSM for most of the study period. In three sites (BC03, MS3523, and MS3552), SSM was overestimated when

it was low and underestimated when it was high, which is consistent with the results from Figure 4. In two sites (MS3559 and MS3603), the scatterplots were distributed along the 1:1 red line. When the same parameters were applied, different validation sites yielded different results.

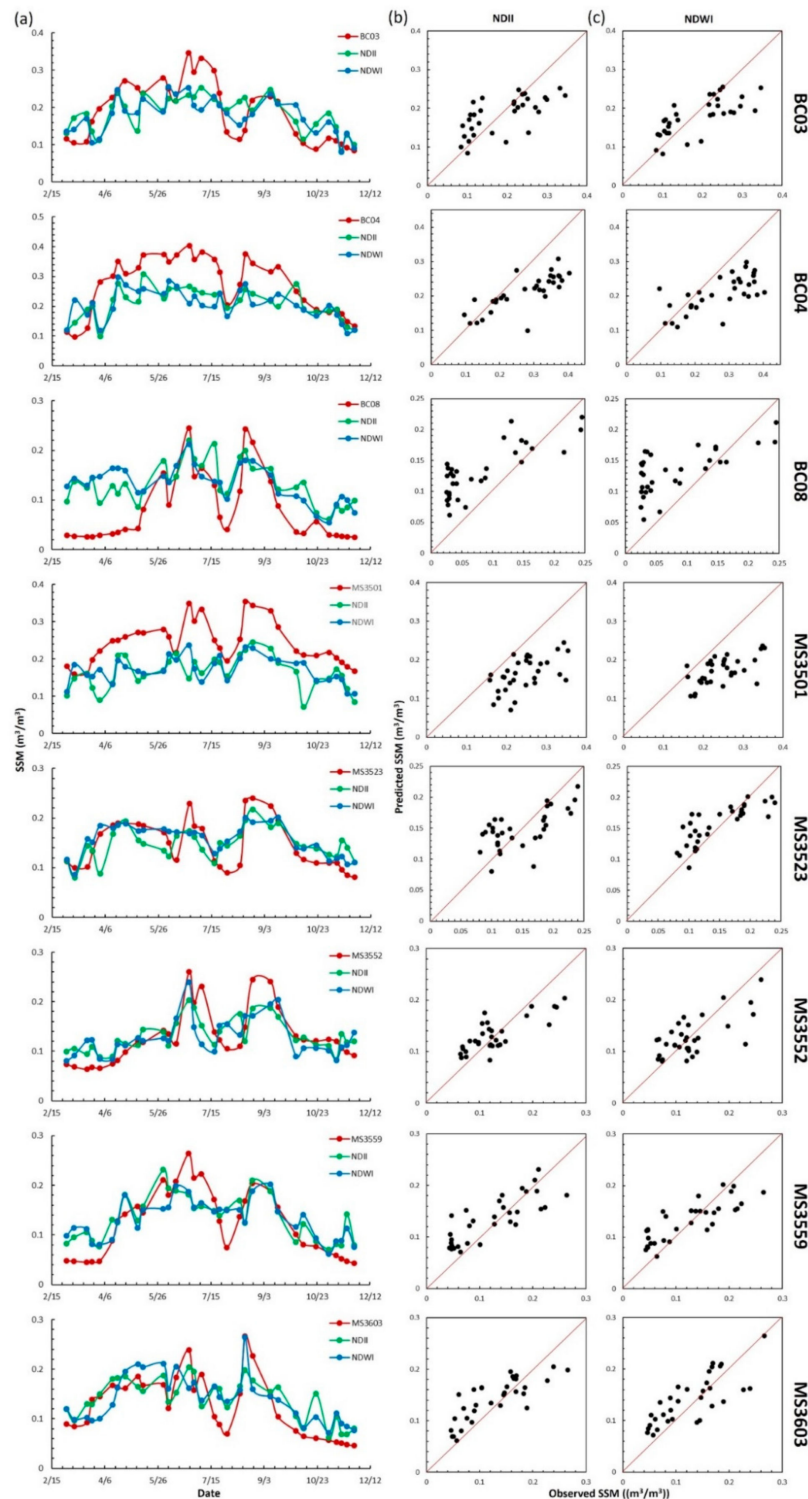


Figure 5. (a) Time series of the observed and predicted surface soil moisture (SSM) values. (b) Scatter plots between the observed and predicted SSM values via normalized difference infrared index (NDII). (c) Scatter plots between the observed and predicted SSM values via normalized difference water index (NDWI) for each validating site.

Figure 6a shows the Landsat 8 false color image using the reflectance band (band1) as red, the shortwave-infrared band (band2) as green, and the near-infrared band (band3) as blue, where red indicates regions with vegetation cover and brown indicates bare soil. From left to right, the images acquired are on 25 May, 18 July, and 22 October. Based on the false color images, in May and October, the study area contained mostly bare soil, while in July, it was fully covered by grass. Figure 6b,d, from left to right, are the generated SSM images when NDII or NDWI were integrated in the sWCM separately. Figure 6c,e show the scatter plots between observed and predicted SSM values when NDII or NDWI were applied in the sWCM, respectively. In spring, both NDII and NDWI overestimated SSM. In summer and autumn, the distribution was along the 1:1 red line and the scatterplots were also accumulated along the 1:1 red line, suggesting that the model works better for soil with vegetation cover compared with bare soil. We observed a spatial-temporal pattern of SSM distribution, with the highest and lowest levels in summer and winter, respectively. Most likely, this is because the active layer starts to thaw in spring, resulting in a rapid increase in SSM. In contrast, in autumn and winter, the soil is mostly frozen, with decreased SSM levels. In spring, the eastern part of the study area showed relatively high SSM values when compared to the western part, while in summer, SSM was lowest in the central part. In winter, the lowest levels were observed for the central and eastern parts. Both images generated by NDII-sWCM and NDWI-sWCM illustrate the same distribution. The NDII-sWCM show lower SSM values compared to the NDWI-sWCM for spring, summer, and autumn.

Although the model proposed in this study achieved good results in the grassland area in TP, we recognize that there are some uncertainties. First, there were uncertainties from satellite measurements, as the MODIS solar bands have associated atmospheric uncertainties. Second, some uncertainties were associated with the ground observations, mainly caused by technique design and experimental design, although calibration and validation were conducted. Third, we estimated the backscattering of the vegetation canopy mainly based on the VWC, but there are other factors that also affect the surface backscattering of active microwave signals such as soil surface roughness. Fourth, the WCM only considers the surface backscattering composed of backscattering from soil and vegetation and assumes there is no reflection within the vegetation canopy. Such assumption can, however, not be made for the “real world”. Soil texture and soil roughness are important factors that affect the backscattering of C-band signals, and omitting such factors may cause uncertainties in the retrieved SSM values when there is a vegetation cover. In addition, both NDII-sWCM and NDWI-sWCM were more suitable when there was a vegetation cover, and the model may need to be revised in this regard. From the scatter plots shown in Figure 4a, we recognized that sWCM underestimates SSM under high SSM conditions in summer and overestimates SSM under low SSM conditions in spring and autumn. The uncertainties within field experiments may induce the monitoring errors. From time series shown in Figure 5a, we see that although the average in situ SSM value is relatively high in summer, for each sampling site the SSM observations vary a lot. There are days for some sites with extremely low SSM values, while other sites with relatively high SSM observations. Besides that, both MODIS and Sentinel-1A only measure the land surface properties, there may be a delay for surface condition change caused by SSM, and it may not be timely observed by satellite sensors. Although the soil temperature is above 0 °C in March and November within the study area, there may exist ice crystals in the soil, the heat absorption or release within the phase change of water may also affect SSM monitoring. In this study, we analyzed the study period together, while the empirical parameters in the sWCM varies under different conditions. If different seasons were studied separately, the monitoring results may be improved.

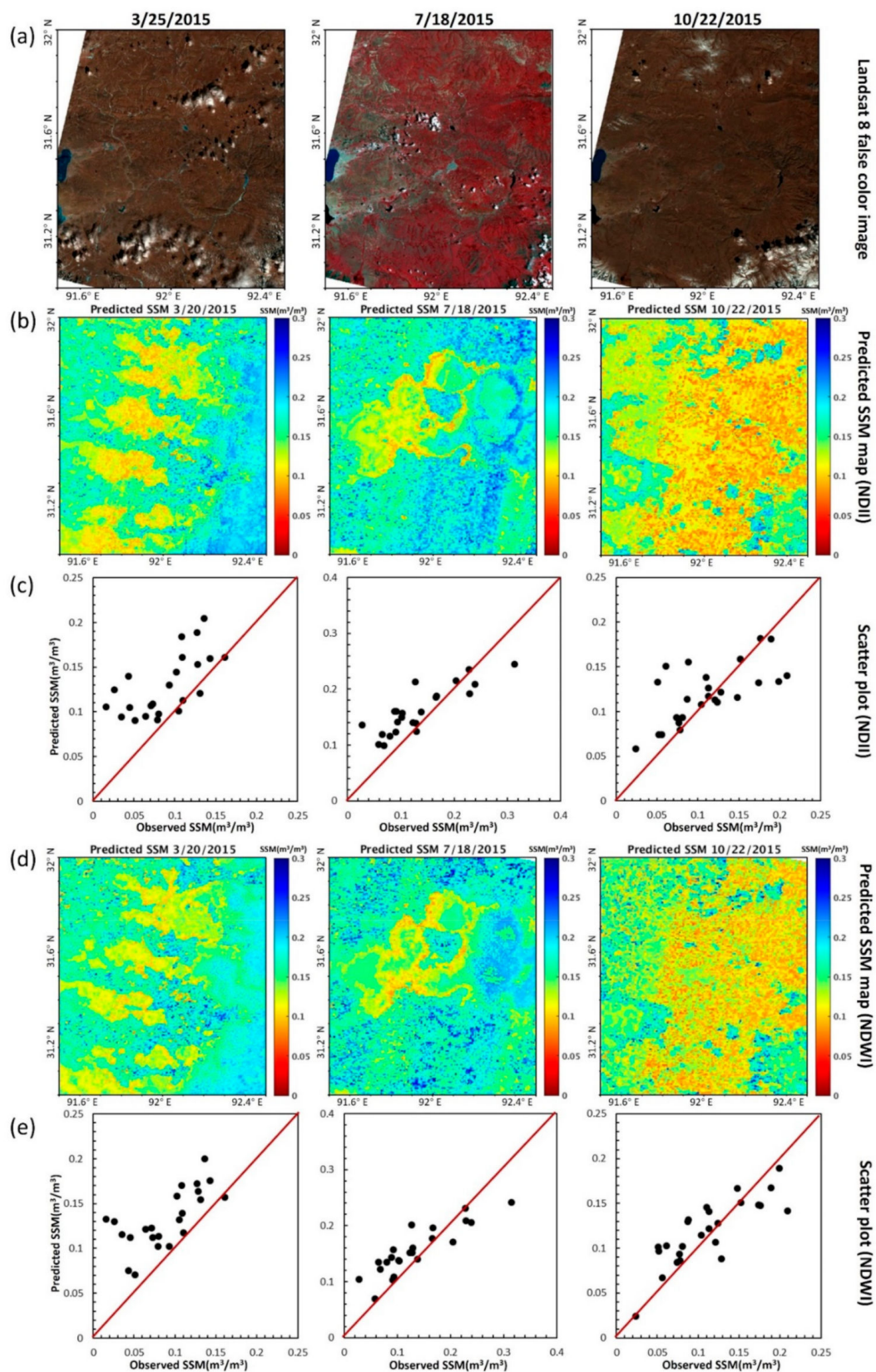


Figure 6. (a) Landsat 8 false color images, (b) normalized difference infrared index (NDII)-retrieved surface soil moisture (SSM) map, (c) scatter-plot between observed and predicted SSM values by NDII, (d) normalized difference water index (NDWI)-retrieved surface soil moisture (SSM) map, (e) scatter plot between observed and predicted SSM values by NDWI on 20 March, 18 July, 22 October, respectively.

5. Conclusions

We mapped SSM at a 500-m resolution for a vegetated area (grassland) of the TP during the non-frozen period (March to November in 2015), combining TERRA MODIS and Sentinel-1 SAR products using the sWCM proposed in this study. The method is based on the relationship between SSM and SAR C-band backscattering, which is based on the soil dielectric variation due to changes in the water content. The impact of vegetation canopy backscattering on the signal SAR received can be dealt with by integrating two VIs (NDII and NDWI) into the WCM, resulting in the models NDII-sWCM and NDWI-sWCM. Both models are well suited for vegetation SSM monitoring, with NDII-sWCM showing better results.

The main contributions of this study are: 1) monitoring of the SSM in a high-latitude permafrost region by combining optical and microwave products during the non-frozen period; 2) elimination of the effects of vegetation canopy backscattering on SAR by assimilating two VIs in the original WCM, resulting in the two simplified water-cloud models NDII-sWCM and NDWI-sWCM. The retrieved SSM values were validated by in situ measurements from CTP-SMTMN. Both NDII and NDWI can be applied in the sWCM to retrieve SSM values for vegetated areas; 3) determination of the temporal and spatial patterns of SSM within the study area from March to November 2015. The central TP showed the highest values in summer and the lowest ones in winter, indicating that the spatial distribution of SSM varies throughout the year. The retrieved 500-m SSM values for vegetated areas are of great importance for further ecosystem and climate research over TP, since the soil water content plays a key role in the water cycle and energy transfer between land and atmosphere via evapotranspiration.

Author Contributions: C.X. designed the experiment, analyzed the data and wrote the manuscript. J.J.Q., X.H. and D.W. revised the manuscript. All authors have read and agreed to the published version of the manuscript.

Funding: This research received no external funding.

Acknowledgments: This study was supported by the USGS Biologic Carbon Sequestration Program entitled “Establish a soil moisture monitoring and forecasting demonstration system by integrating satellite remote sensing measurements, in situ observations and model simulations”. The authors express sincere thanks to Prof. Yang from Tsinghua University providing the in situ soil moisture data of CTP-SMTMN network. We also thank the editors and reviewers for their valuable comments to improve this manuscript.

Conflicts of Interest: The authors declare no conflict of interest.

Abbreviations

AIEM	Advanced Integral Equation Model
ALOS	Advanced Land Observation Satellite
AMSR-E	the Advanced Microwave Scanning Radiometer for EOS
ANN	Artificial Neural Network
CAS	Chinese Academy of Sciences
COSMOS	The COsmic-ray Soil Moisture Observing System
CTP-SMTMN	Multiscale Soil Moisture and Temperature Monitoring Network on the central Tibetan Plateau
DAM	Data Assimilation and Modeling Center for Tibetan Multi-spheres
DEM	Digital Elevation Map
EOS	Earth Observing System
ERS	European Remote-Sensing Satellite
ESA	European Space Agency
LSM	Land Surface Model
MODIS	Moderate Resolution Imaging Spectroradiometer
NASA	National Aeronautics and Space Administration
NDII	Normalized Difference Infrared Index
NDVI	Normalized Difference Vegetation Index
NDWI	Normalized Difference Water Index
PALSAR	the Phased Array type L-band Synthetic Aperture Radar
R^2	Correlation of determination

RMSE	Root Mean Squared Error
ubRMSE	unbiased RMSE
SAR	Synthetic Aperture Radar
SNAP	Sentinel Application Platform
SMAP	Soil Moisture Active Passive
SMOS	Soil Moisture and Ocean Salinity
SM	Soil Moisture
SSM	Surface Soil Moisture
SSM/I	the Special Sensor Microwave Imager
SMMR	Scanning Multi-channel Microwave Radiometer
ST	Soil Temperature
SVM	Support Vector Machine
TSX	TerraSAR X-band
TP	Tibetan Plateau
VI	Vegetation Index
VWC	Vegetation Water Content
WCM	Water Cloud Model
sWCM	simplified Water Cloud Model

References

1. Koster, R.D.; Dirmeyer, P.A.; Guo, Z.; Bonan, G.; Chan, E.; Cox, P.; Gordon, C.T.; Kanae, S.; Kowalczyk, E.; Lawrence, D.; et al. Regions of strong coupling between soil moisture and precipitation. *Science* **2004**, *305*, 1138–1140. [[CrossRef](#)] [[PubMed](#)]
2. Paris Anguela, T.; Zribi, M.; Hasenauer, S.; Habets, F.; Loumagne, C. Analysis of surface and root-zone soil moisture dynamics with ERS scatterometer and the hydrometeorological model SAFRAN-ISBA-MODCOU at Grand Morin watershed (France). *Hydrol. Earth Syst. Sci.* **2008**, *12*, 1415–1424. [[CrossRef](#)]
3. Saux-Picart, S.; Otlé, C.; Decharme, B.; André, C.; Zribi, M.; Perrier, A.; Coudert, B.; Boulain, N.; Cappelaere, B.; Descroix, L.; et al. Water and energy budgets simulation over the AMMA-Niger super-site spatially constrained with remote sensing data. *J. Hydrol.* **2009**, *375*, 287–295. [[CrossRef](#)]
4. Barrett, B.; Petropoulos, G.P. *Satellite remote sensing of surface soil moisture. Remote Sens. Energy Fluxes Soil Moisture Content*; CRC Press Taylor & Francis Group: Boca Raton, FL, USA, 2013.
5. Elefante, S.; Wagner, W.; Briese, C.; Cao, S.; Naeimi, V. High-performance computing for soil moisture estimation. In Proceedings of the 2016 Conference on Big Data from Space (BiDS'16), Santa Cruz de Tenerife, Spain, 15–17 March 2016; pp. 95–98.
6. Petropoulos, G.P.; Ireland, G.; Barrett, B. Surface soil moisture retrievals from remote sensing: Current status, products & future trends. *Phys. Chem. Earth Parts A B C* **2015**, *83*, 36–56.
7. Zeng, J.; Li, Z.; Chen, Q.; Bi, H.; Qiu, J.; Zou, P. Evaluation of remotely sensed and reanalysis soil moisture products over the Tibetan Plateau using in-situ observations. *Remote Sens. Environ.* **2015**, *163*, 91–110. [[CrossRef](#)]
8. Xu, C.; Qu, J.; Hao, X.; Cosh, M.; Prueger, J.; Zhu, Z.; Gutengberg, L. Downscaling of surface soil moisture retrieval by combining MODIS/Landsat and in situ measurements. *Remote Sens.* **2018**, *10*, 210. [[CrossRef](#)]
9. Wang, L.; Qu, J.J. Satellite remote sensing applications for surface soil moisture monitoring: A review. *Front. Earth Sci. China* **2009**, *3*, 237–247. [[CrossRef](#)]
10. Pablos, M.; González-Zamora, Á.; Sánchez, N.; Martínez-Fernández, J. Assessment of root zone soil moisture estimations from SMAP, SMOS and MODIS observations. *Remote Sens.* **2018**, *10*, 981. [[CrossRef](#)]
11. Shrestha, P.; Kurtz, W.; Vogel, G.; Schulz, J.P.; Sulis, M.; Hendricks Franssen, H.J.; Kollet, S.; Simmer, C. Connection Between Root Zone Soil Moisture and Surface Energy Flux Partitioning Using Modeling, Observations, and Data Assimilation for a Temperate Grassland Site in Germany. *J. Geophys. Res. Biogeosci.* **2018**, *123*, 2839–2862. [[CrossRef](#)]
12. Scoville, N.; Aussel, H.; Brusa, M.; Capak, P.; Carollo, C.M.; Elvis, M.; Giavalisco, M.; Guzzo, L.; Hasinger, G.; Impey, C.; et al. The cosmic evolution survey (COSMOS): Overview. *Astrophys. J. Suppl. Ser.* **2007**, *172*, 1. [[CrossRef](#)]
13. Ångström, A. The albedo of various surfaces of ground. *Geografiska Ann.* **1925**, *7*, 323–342.

14. Jackson, R.D.; Idso, S.B.; Reginato, R.J. Calculation of evaporation rates during the transition from energy-limiting to soil-limiting phases using albedo data. *Water Resour. Res.* **1976**, *12*, 23–26. [[CrossRef](#)]
15. Sadeghi, A.M.; Hancock, G.D.; Waite, W.P.; Scott, H.D.; Rand, J.A. Microwave measurements of moisture distributions in the upper soil profile. *Water Resour. Res.* **1984**, *20*, 927–934. [[CrossRef](#)]
16. Carlson, T. An overview of the “triangle method” for estimating surface evapotranspiration and soil moisture from satellite imagery. *Sensors* **2007**, *7*, 1612–1629. [[CrossRef](#)]
17. Verstraeten, W.W.; Veroustraete, F.; van der Sande, C.J.; Grootaers, I.; Feyen, J. Soil moisture retrieval using thermal inertia, determined with visible and thermal spaceborne data, validated for European forests. *Remote Sens. Environ.* **2006**, *101*, 299–314. [[CrossRef](#)]
18. Boerner, W.M.; Morisaki, J.J. From airborne via drones to space-borne polarimetric-interferometric SAR environmental stress-change monitoring—Comparative assessment of applications. In Proceedings of the 15th International Conference on Microwaves, Radar and Wireless Communications (IEEE Cat. No. 04EX824), Warsaw, Poland, 17–19 May 2004; IEEE: Piscataway, NJ, USA, 2004; Volume 3, pp. 901–904.
19. Das, N.N.; Entekhabi, D.; Kim, S.; Yueh, S.; O’Neill, P. Combining SMAP and Sentinel data for high-resolution Soil Moisture product. In Proceedings of the 2016 IEEE International Geoscience and Remote Sensing Symposium (IGARSS), Beijing, China, 10–15 July 2016; IEEE: Piscataway, NJ, USA, 2016; pp. 129–131.
20. Entekhabi, D.; Njoku, E.G.; O’Neill, P.E.; Kellogg, K.H.; Crow, W.T.; Edelstein, W.N.; Entin, J.K.; Goodman, S.D.; Jackson, T.J.; Johnson, J.; et al. The soil moisture active passive (SMAP) mission. *Proc. IEEE* **2010**, *98*, 704–716. [[CrossRef](#)]
21. Kerr, Y.H.; Waldteufel, P.; Wigneron, J.P.; Martinuzzi, J.A.M.J.; Font, J.; Berger, M. Soil moisture retrieval from space: The Soil Moisture and Ocean Salinity (SMOS) mission. *IEEE Trans. Geosci. Remote Sens.* **2001**, *39*, 1729–1735. [[CrossRef](#)]
22. Njoku, E.G.; Chan, S.K. Vegetation and surface roughness effects on AMSR-E land observations. *Remote Sens. Environ.* **2006**, *100*, 190–199. [[CrossRef](#)]
23. Pasolli, L.; Notarnicola, C.; Bertoldi, G.; Bruzzone, L.; Remelgado, R.; Greifeneder, F.; Niedrist, G.; Della Chiesa, S.; Tappeiner, U.; Zebisch, M. Estimation of soil moisture in mountain areas using SVR technique applied to multiscale active radar images at C-band. *IEEE J. Sel. Top. Appl. Earth Observ. Remote Sens.* **2015**, *8*, 262–283. [[CrossRef](#)]
24. Joseph, A.T.; van der Velde, R.; O’Neill, P.E.; Lang, R.; Gish, T. Effects of corn on C-and L-band radar backscatter: A correction method for soil moisture retrieval. *Remote Sens. Environ.* **2010**, *114*, 2417–2430. [[CrossRef](#)]
25. Jonard, F.; Weihermuller, L.; Jadoon, K.Z.; Schwank, M.; Vereecken, H.; Lambot, S. Mapping field-scale soil moisture with L-band radiometer and ground-penetrating radar over bare soil. *IEEE Trans. Geosci. Remote Sens.* **2011**, *49*, 2863–2875. [[CrossRef](#)]
26. Balenzano, A.; Mattia, F.; Satalino, G.; Pauwels, V.; Snoeij, P. SMOSAR algorithm for soil moisture retrieval using Sentinel-1 data. In Proceedings of the 2012 IEEE International Geoscience and Remote Sensing Symposium, Munich, Germany, 22–27 July 2012; IEEE: Piscataway, NJ, USA, 2012; pp. 1200–1203.
27. Gherboudj, I.; Magagi, R.; Berg, A.A.; Toth, B. Soil moisture retrieval over agricultural fields from multi-polarized and multi-angular RADARSAT-2 SAR data. *Remote Sens. Environ.* **2011**, *115*, 33–43. [[CrossRef](#)]
28. Gruber, A.; Wagner, W.; Hegyiova, A.; Greifeneder, F.; Schläffer, S. Potential of Sentinel-1 for high-resolution soil moisture monitoring. In Proceedings of the 2013 IEEE International Geoscience and Remote Sensing Symposium-IGARSS, Melbourne, Australia, 21–26 July 2013; IEEE: Piscataway, NJ, USA, 2013; pp. 4030–4033.
29. Koyama, C.N.; Schneider, K. Soil moisture retrieval under vegetation using dual polarized PALSAR data. In Proceedings of the 2011 IEEE International Geoscience and Remote Sensing Symposium, Vancouver, BC, Canada, 24–29 July 2011; IEEE: Piscataway, NJ, USA, 2011; pp. 1059–1062.
30. Ponnurangam, G.G.; Rao, Y.S. Soil moisture mapping using ALOS PALSAR and ENVISAT ASAR data over India. In Proceedings of the 2011 3rd International Asia-Pacific Conference on Synthetic Aperture Radar (APSAR), Seoul, Korea, 26–30 September 2011; IEEE: Piscataway, NJ, USA, 2011; pp. 1–4.
31. Bai, X.; He, B.; Li, X.; Zeng, J.; Wang, X.; Wang, Z.; Su, Z. First assessment of Sentinel-1A data for surface soil moisture estimations using a coupled water cloud model and advanced integral equation model over the Tibetan Plateau. *Remote Sens.* **2017**, *9*, 714. [[CrossRef](#)]

32. Gao, Q.; Zribi, M.; Escorihuela, M.; Baghdadi, N. Synergetic use of Sentinel-1 and Sentinel-2 data for soil moisture mapping at 100 m resolution. *Sensors* **2017**, *17*, 1966. [[CrossRef](#)]
33. Hornacek, M.; Wagner, W.; Sabel, D.; Truong, H.L.; Snoeij, P.; Hahmann, T.; Diedrich, E.; Doubková, M. Potential for high resolution systematic global surface soil moisture retrieval via change detection using Sentinel-1. *IEEE J. Sel. Top. Appl. Earth Observ. Remote Sens.* **2012**, *5*, 1303–1311. [[CrossRef](#)]
34. Attema, E.P.W.; Ulaby, F.T. Vegetation modeled as a water cloud. *Radio Sci.* **1978**, *13*, 357–364. [[CrossRef](#)]
35. Paloscia, S.; Pettinato, S.; Santi, E.; Notarnicola, C.; Pasolli, L.; Reppucci, A. Soil moisture mapping using Sentinel-1 images: Algorithm and preliminary validation. *Remote Sens. Environ.* **2013**, *134*, 234–248. [[CrossRef](#)]
36. Sabel, D.; Bartsch, A.; Schlaffer, S.; Klein, J.P.; Wagner, W. Soil moisture mapping in permafrost regions—An outlook to Sentinel-1. In Proceedings of the 2012 IEEE International Geoscience and Remote Sensing Symposium, Munich, Germany, 22–27 July 2012; IEEE: Piscataway, NJ, USA, 2012; pp. 1216–1219.
37. Wang, S.G.; Li, X.; Han, X.J.; Jin, R. Estimation of surface soil moisture and roughness from multi-angular ASAR imagery in the Watershed Allied Telemetry Experimental Research (WATER). *Hydrol. Earth Syst. Sci.* **2011**, *15*, 1415–1426. [[CrossRef](#)]
38. Wagner, W.; Sabel, D.; Doubkova, M.; Bartsch, A.; Pathe, C. The potential of Sentinel-1 for monitoring soil moisture with a high spatial resolution at global scale. In Proceedings of the Symposium of Earth Observation and Water Cycle Science, Frascati, Italy, 18–20 November 2009.
39. Kumar, K.; Suryanarayana Rao, H.P.; Arora, M.K. Study of water cloud model vegetation descriptors in estimating soil moisture in Solani catchment. *Hydrol. Process.* **2015**, *29*, 2137–2148. [[CrossRef](#)]
40. Baghdadi, N.; El Hajj, M.; Zribi, M.; Bousbih, S. Calibration of the water cloud model at C-band for winter crop fields and grasslands. *Remote Sens.* **2017**, *9*, 969. [[CrossRef](#)]
41. Balenzano, A.; Mattia, F.; Satalino, G.; Davidson, M.W. Dense temporal series of C-and L-band SAR data for soil moisture retrieval over agricultural crops. *IEEE J. Sel. Top. Appl. Earth Observ. Remote Sens.* **2010**, *4*, 439–450. [[CrossRef](#)]
42. Lievens, H.; Verhoest, N.E. On the retrieval of soil moisture in wheat fields from L-band SAR based on water cloud modeling, the IEM, and effective roughness parameters. *IEEE Geosci. Remote Sens. Lett.* **2011**, *8*, 740–744. [[CrossRef](#)]
43. Li, J.; Wang, S.; Gunn, G.; Joosse, P.; Russell, H.A. A model for downscaling SMOS soil moisture using Sentinel-1 SAR data. *Int. J. Appl. Earth Observ. Geoinf.* **2018**, *72*, 109–121. [[CrossRef](#)]
44. Mattia, F.; Satalino, G.; Balenzano, A.; Rinaldi, M.; Steduto, P.; Moreno, J. Sentinel-1 for wheat mapping and soil moisture retrieval. In Proceedings of the 2015 IEEE International Geoscience and Remote Sensing Symposium (IGARSS), Milan, Italy, 26–31 July 2015; IEEE: Piscataway, NJ, USA, 2015; pp. 2832–2835.
45. Notarnicola, C.; Posa, F. Inferring vegetation water content from C-and L-band SAR images. *IEEE Trans. Geosci. Remote Sens.* **2007**, *45*, 3165–3171. [[CrossRef](#)]
46. Yadav, V.P.; Prasad, R.; Bala, R.; kumar Vishwakarma, A. Estimation of soil moisture through water cloud model using sentinel-1A SAR data. In Proceedings of the IGARSS 2019–2019 IEEE International Geoscience and Remote Sensing Symposium, Okohama, Japan, 28 July–2 August 2019; IEEE: Piscataway, NJ, USA, 2019; pp. 6961–6964.
47. Zhuo, W.; Huang, J.; Li, L.; Zhang, X.; Ma, H.; Gao, X.; Xiao, X. Assimilating soil moisture retrieved from Sentinel-1 and Sentinel-2 data into WOFOST model to improve winter wheat yield estimation. *Remote Sens.* **2019**, *11*, 1618. [[CrossRef](#)]
48. Wang, L.; He, B.; Bai, X.; Xing, M. Assessment of Different Vegetation Parameters for Parameterizing the Coupled Water Cloud Model and Advanced Integral Equation Model for Soil Moisture Retrieval Using Time Series Sentinel-1A Data. *Photogramm. Eng. Remote Sens.* **2019**, *85*, 43–54. [[CrossRef](#)]
49. Bao, Y.; Lin, L.; Wu, S.; Deng, K.A.K.; Petropoulos, G.P. Surface soil moisture retrievals over partially vegetated areas from the synergy of Sentinel-1 and Landsat 8 data using a modified water-cloud model. *Int. J. Appl. Earth Observ. Geoinf.* **2018**, *72*, 76–85. [[CrossRef](#)]
50. Ceccato, P.; Flasse, S.; Tarantola, S.; Jacquemoud, S.; Grégoire, J.M. Detecting vegetation leaf water content using reflectance in the optical domain. *Remote Sens. Environ.* **2001**, *77*, 22–33. [[CrossRef](#)]

51. Chen, D.; Jackson, T.J.; Li, F.; Cosh, M.H.; Walthall, C.; Anderson, M. Estimation of vegetation water content for corn and soybeans with a normalized difference water index (NDWI) using Landsat Thematic Mapper data. In Proceedings of the IGARSS 2003 IEEE International Geoscience and Remote Sensing Symposium (IEEE Cat. No. 03CH37477), Toulouse, France, 21–25 July 2003; IEEE: Piscataway, NJ, USA, 2003; Volume 4, pp. 2853–2856.
52. Chen, D.; Huang, J.; Jackson, T.J. Vegetation water content estimation for corn and soybeans using spectral indices derived from MODIS near-and short-wave infrared bands. *Remote Sens. Environ.* **2005**, *98*, 225–236. [[CrossRef](#)]
53. Gao, B.C. NDWI—A normalized difference water index for remote sensing of vegetation liquid water from space. *Remote Sens. Environ.* **1996**, *58*, 257–266. [[CrossRef](#)]
54. Hunt, E.R., Jr.; Li, L.; Yilmaz, M.T.; Jackson, T.J. Comparison of vegetation water contents derived from shortwave-infrared and passive-microwave sensors over central Iowa. *Remote Sens. Environ.* **2011**, *115*, 2376–2383. [[CrossRef](#)]
55. Xu, C.; Qu, J.J.; Hao, X.; Cosh, M.H.; Zhu, Z.; Gutenberg, L. Monitoring crop water content for corn and soybean fields through data fusion of MODIS and Landsat measurements in Iowa. *Agric. Water Manag.* **2020**, *227*, 105844. [[CrossRef](#)]
56. Zarco-Tejada, P.J.; Rueda, C.A.; Ustin, S.L. Water content estimation in vegetation with MODIS reflectance data and model inversion methods. *Remote Sens. Environ.* **2003**, *85*, 109–124. [[CrossRef](#)]
57. Jackson, T.J.; Chen, D.; Cosh, M.; Li, F.; Anderson, M.; Walthall, C.; Doriaswamy, P.; Hunt, E.R. Vegetation water content mapping using Landsat data derived normalized difference water index for corn and soybeans. *Remote Sens. Environ.* **2004**, *92*, 475–482. [[CrossRef](#)]
58. Wang, L.; Qu, J.J.; Hao, X.; Zhu, Q. Sensitivity studies of the moisture effects on MODIS SWIR reflectance and vegetation water indices. *Int. J. Remote Sens.* **2008**, *29*, 7065–7075. [[CrossRef](#)]
59. Bi, H.; Ma, J.; Zheng, W.; Zeng, J. Comparison of soil moisture in GLDAS model simulations and in situ observations over the Tibetan Plateau. *J. Geophys. Res. Atmos.* **2016**, *121*, 2658–2678. [[CrossRef](#)]
60. Yang, K.; Qin, J.; Zhao, L.; Chen, Y.; Tang, W.; Han, M.; Chen, Z.; Lv, N.; Ding, B.; Wu, H.; et al. A multiscale soil moisture and freeze–thaw monitoring network on the third pole. *Bull. Am. Meteorol. Soc.* **2013**, *94*, 1907–1916. [[CrossRef](#)]
61. Chen, Y.; Yang, K.; Qin, J.; Cui, Q.; Lu, H.; La, Z.; Han, M.; Tang, W. Evaluation of SMAP, SMOS, and AMSR2 soil moisture retrievals against observations from two networks on the Tibetan Plateau. *J. Geophys. Res. Atmos.* **2017**, *122*, 5780–5792. [[CrossRef](#)]



© 2020 by the authors. Licensee MDPI, Basel, Switzerland. This article is an open access article distributed under the terms and conditions of the Creative Commons Attribution (CC BY) license (<http://creativecommons.org/licenses/by/4.0/>).